Experimental characterization of a latent heat storage unit with lithium nitrate inside finned cylinders for assisting solar air heating

Antonio Famiglietti[1,2] and Antonio Lecuona-Neumann [1]

1 Universidad Carlos III de Madrid, Departamento de Ingeniería Térmica y de Fluidos, Leganés, (Spain)

2 Demede Engineering and Research, Madrid (Spain)

Abstract

Thermal energy storage technologies offer a promising solution for reducing the mismatch between heat demand and solar heat supply. Heat storage has huge potential for application in solar facilities for process heat at medium temperatures, nowadays not much explored. In this study, a small-scale latent heat storage unit is implemented and experimentally investigated. Lithium nitrate salt is selected as the storage material for its excellent properties. It is encapsulated inside vertical externally finned cylinders. Air is the heat transfer fluid. The thermal storage unit is integrated into an existing innovative prototype for direct solar heating of air which can provide hot air up to $300 - 400$ °C using a 79.2 m^2 linear Fresnel collector field. TES charge and discharge tests are performed, and they are critically analyised. Results allow the thermal characterization of the storage unit and underpin critical aspects for scaling up. The experimental data obtained are relevant information for the numerical models tuning and validation.

Latent heat storage; solar heat for industrial processes; Linear Fresnel collector; Lithium nitrate; phase change material.

1. Introduction

Solar thermal technologies are a suitable solution for industrial heat demand in the low and medium temperature range, (Sharma *et al.*, 2017). Solar intermittency and variability can preclude matching the solar heat supply with industrial demand, representing an important obstacle to the implementation of solar thermal system at a large scale.

Thermal Energy Storage TES represents a key technology for mitigating this drawback and increasing the dependability of solar thermal systems. Extensive research has been carried out during the last decades on TES applications for low-temperature domestic heating systems as well as for large-scale and high-temperature concentrated solar power CSP. Medium temperature TES, especially suitable for solar heat for industrial process SHIP applications, has received limited attention, despite its high potential. (Crespo *et al.*, 2018) offers an extensive review on TES systems, analyzing the state of the art of technology and materials. The authors highlight the potential of latent heat storage for industrial applications in the range of temperature $150 - 400$ °C.

The use of air as heat transfer fluid is widespread in the industry. Many processes use hot air for drying, curing, finishing a large variety of products, materials, or residues. Process air heating is currently achieved by consuming fossil fuels or electricity, although solar thermal technologies are rising as an interesting alternative.

(Famiglietti *et al.*, 2020) proposes direct air heating inside linear concentrating collectors in order to provide process air at 300 - 400°C, with no need for a primary heat transfer fluid HTF (oil, pressurized water) neither HTF/air heat exchanger. Either linear Fresnel Collectors LFCs or Parabolic Trough Collectors PTCs are suitable for the purpose. In the original layout studied, an automotive turbocharger is coupled with the solar field allowing to minimize or avoid the pumping power required, as numerically demonstrated in a further study, (Famiglietti *et al.*, 2021). A first-generation prototype of the Turbo-assisted Solar Air Heater T-SAH is currently installed at Carlos III University Campus of Madrid, Fig.1 offers a scheme.

In this study, an experimental medium-temperature latent heat storage unit, integrated into the existing T-SAH prototype, has been designed, built, and tested. The Lithium Nitrate salt LiNO$_3$ has been selected as storage

material due to its suitable melting temperature of 254 °C and its high specific latent heat of 360 kJ/kg, about three times higher than other alternatives.

2. Experimental setup

The heat storage unit is installed on a building rooftop of the Carlos III University of Madrid. It is integrated into the existing experimental prototype devised for solar air heating T-SAH, Fig.1. The innovative T-SAH uses three first generation commercial linear Fresnel collectors (Solatom™) in series, reaching 79.2 m^2 of capturing area. Two parallel electrical blowers *ac* (Elektor SD22 FU 80/1,1) fed by a frequency converter are connected to the inlet of the turbo-compressor *c*. A small-size automotive turbocharger is used for increasing air density inside the solar field, this way reducing pressure drops, and recovering compressing power through the attached turbine *e*. The air circuit is instrumented with class A thermocouples type K, and pressure sensors, having respectively estimated total uncertainty of ±2.0 °C and ±25 mbar, while an airflow sensor with a total uncertainty of ±3% (Schmidt 30.015 MPM) is installed at the atmospheric inlet. Piping is thermally insulated using mineral wool and glass fiber. The T-SAH prototype has been analysed in details in (Famiglietti and Lecuona, 2021a) and (Famiglietti and Lecuona, 2021b).

The TES unit is mounted downstream of the turbine, Fig.1. A manual switching valve connects the TES directly to the solar air heater, as required during the charging test, which can be bypassed if required.
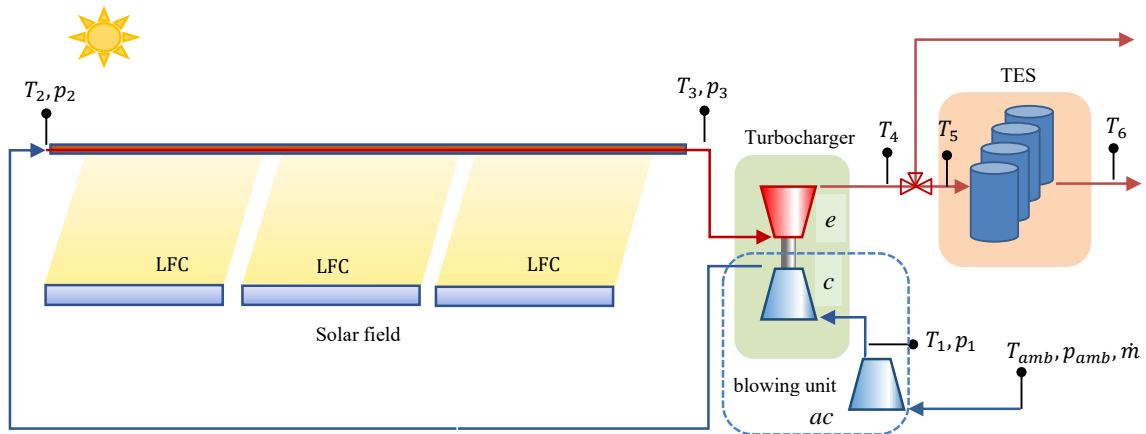

Fig. 1. Experimental setup scheme, Linear Fresnel Collector LFC, auxiliary compressor ac, turbo-compressor c, turbine e, thermal storage unit TES.

A "shell and tube" design is chosen for the TES heat exchanger configuration, in a single row layout. There, the air flows inside a straight channel across four vertical tubes filled with the phase change material (LiNO$_3$). Commercial tubes with round transversal fins appeared as the best solution for improving the heat transfer rate in the airflow side, keeping a low-cost and easy manufacturing. For the air channel, some air conditioning ducts are considered due to the low cost and their widespread availability on the market as they are used for air conditioning in buildings.

Fig. 2 (a) reports a 3D drawing of the TES core. An air channel with a square cross-section of 600 mm and a length of 500 mm is chosen. The lithium nitrate salt is filled inside four externally finned cylinders made of stainless steel, having an internal diameter of 76.1 mm, 2.9 mm wall thickness, an overall height of 570 mm, and a finned height of 490 mm. The cylinders are externally finned with welded helicoidal corrugated fins of carbon steel, with a height of 35 mm and thickness of 0.7 mm. The distance between fins is 6 mm. The upper and lower no-fins apertures are closed with removable flanges. The cylinders are placed vertically and adjacent one to another, in parallel to the perpendicular airflow, Fig. 2(a).

One of the inner four cylinders is instrumented with type K thermocouples, Fig. 2(b). They are placed in the

central vertical axis, at the upper as well as at the lower part and in the middle. Additional thermocouples were placed on the horizontal plane at the medium height cross-section to detect temperature gradients in the horizontal radial direction, Fig. 2 (b). To correctly position the thermocouples inside the tube a thin structure is needed as shown in Fig. 3(b). They are fixed on the upper flange and positioned with the aid of three separators made of stainless steel and 1 mm thickness, then aligned using two vertical threaded rods, Fig.3(b). Two thermocouples measure air temperature at the inlet and outlet of the TES channel.
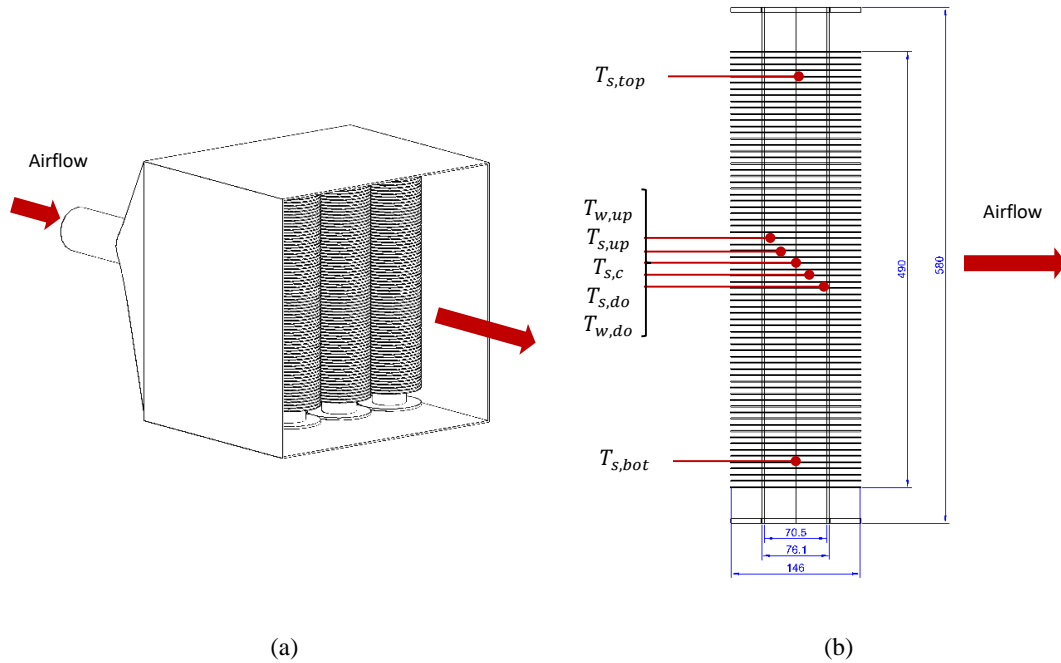

| (a) | (b) |

Fig. 2. TES layout and finned cylinder. (a) Finned cylinders inside insulated the air channel. (b) Finned cylinder instrumented.

Fig. 3(a) depicts the whole air channel. A 100 mm diameter round duct connects the TES core with the T-SAH outlet (turbine exit).

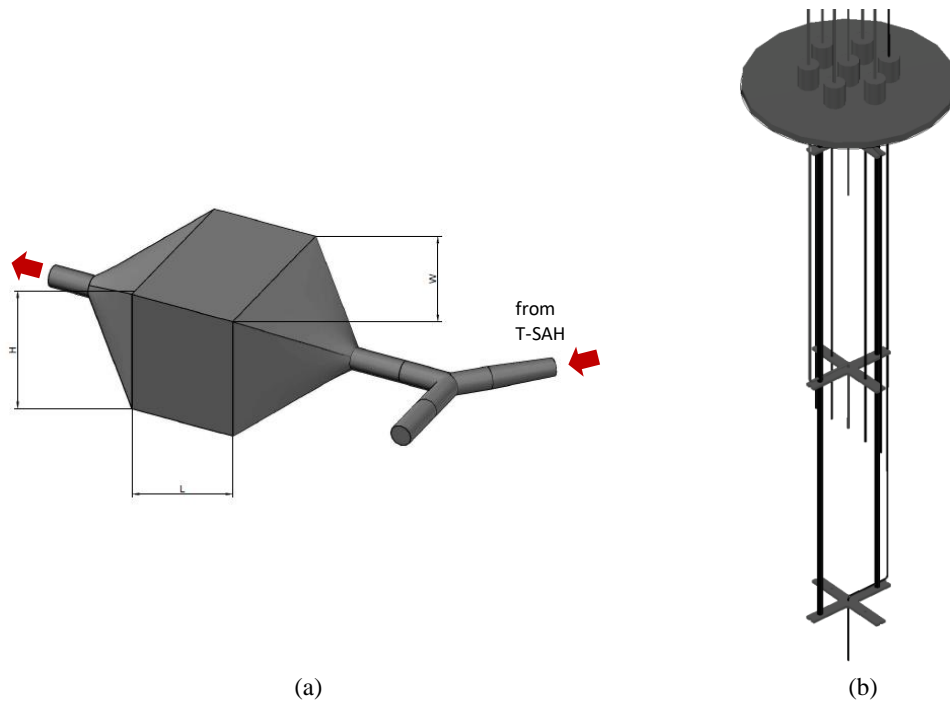| (a) | (b) |

Fig. 3. TES air channel. (a) 3D view. (b) Thermocouples inside the instrumented tube, with separators plates.

The TES unit is assembled and is integrated downstream the T-SAH turbine. The finned cylinders are filled with $LiNO_3$ in a fine granular state. A second filling operation was devised after the first melt. Fig. 4 (a) shows a single finned cylinder partially filled with $LiNO_3$. The thermocouples assembly is prepared as in Fig. 4(b), to be inserted into the instrumented cylinder before filling it with salt.
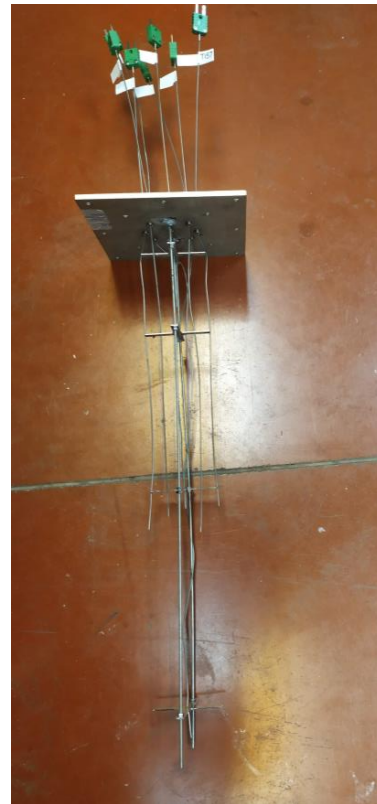
(a)   (b)

Fig. 4. TES preparation. (a) Finned cylinder; (b) Thermocouples and supporting structure.

Then the four cylinders sealed with their flanges are assembled inside the square duct as in Fig. 5(a). Once the TES core was assembled, it has been covered with a mineral wool insulation of 150 mm thickness and covered with aluminum foil, Fig. 5(b). The connection duct with the turbine exit is installed and insulated.

<table>
<tr><td>(a)</td><td>(b)</td></tr>
</table>

Fig. 5. TES components. (a) Cylinders and inside the square duct, (b) insulated TES box, air duct before insulation.

Each of the four cylinders is initially filled with 2.6 kg of commercial $LiNO_3$ in a granular state, occupying 100% of the internal volume of 2.18 L, thus with an average density of 1,190 kg/m^3. The weight of an empty finned cylinder is 8.9 kg. The density of solid salt at room temperature is higher, although in the literature the exact value diverges from one source to another, between 1,780 kg/m^3 (Tamme, R. et al. 2008) to 2,380 kg/m^3 (Chemicalbook). For that reason, a first melting and solidifying cycle has been carried out, before inspecting inside the cylinders, as reported in Fig. 6. It shows as the solidified salt fills around 60% of cylinder volume, having a density of 1,990 kg/m^3 at room temperature.

<table>
<tr><td>(a)</td><td>(b)</td></tr>
</table>

Fig. 6. Finned cylinder inspection after first melting/solidifying cycle. (a) Partially filled volume, (b) empty height.

An additional amount of salt of 0.770 kg is filled in each cylinder, reaching a total amount of 3.37 kg of salt per cylinder and 13.48 kg for the whole TES. A melting and solidifying cycle has been repeated before checking again the status of the salt, reported in Fig. 7.

The filled volume with solid salt is now 77% of the total height. The air gap in the upper part of the cylinder allows the volume to increase from a solid to a liquid state. Considering a liquid density at 300 °C of 1,753 kg/m^3, the salt volume at the liquid state is expected to reach 90% of the internal cylinder volume, avoiding the risk of leakage from the upper flange or its rupture. In Fig. 7(a) it can be noticed that during the solidification process, the contracting salt can originate an empty region in the center of the material block similar to a hole. This is caused by the progression towards the axis of the solidification front and the fall of the inner liquid fraction.

(a)   (b)

Fig. 7. Finned cylinder inspection after the second melting/solidifying cycle with increased salt content. (a) Non-uniform salt block, (b) Empty height showing the thermocouple brackets.

3. Results

Two representative tests were devised for qualitative characterization of the TES unit. The first one allows to obtain the charging and discharging curves and features. The second test reveals the effect of the TES unit on the delivery air temperature of the combined T-SAH and TES prototypes.

Fig. 8 shows the charging and discharging test results. The TES is initially disconnected from the T-SAH. During more than one hour the T-SAH is run alone, with the solar field in tracking mode. When the exit turbine temperature T_4, higher than 300 °C, is reached, then the TES unit is connected, and the hot airflow starts to heat the finned cylinders. Fig.8 reports the air temperature at the TES inlet T_5 is (a). Due to T-SAH features and sun availability, T_5 is not constant during the charging period, but varies between 300 °C and 350 °C. The temperature of the salt T_s measured at three points of the medium-height transversal cross-section according to Fig. 9(b) is reported in Fig. 8(a). A sensible solid heating period of 65 - 70 min with a rapid temperature rise proceeds the melting process, which lasts approximatively 70 min. Once the salt is completely molten, the temperature starts to rise again during a liquid sensible heating, going up to 280 °C. Air at the TES outlet holds the temperature T_6, also reported in Fig.8 (a), which shows a smoother time profile than the salt temperature T_s.

Before running the discharging test, the solar field is defocused, and the TES is disconnected from T-SAH for a short time. Meanwhile, the air flowing into the T-SAH cools progressively the components of the air circuit (pipes, receiver, turbocharger). When the air temperature at the turbine outlet T_4 drops below the salt temperature ($\sim$ 200 °C) the TES is connected again to the T-SAH, and the airflow starts to cool the cylinders. The solidification process lasts around 75 min, with inlet air temperature T_5 dropping from $\sim$200 °C to $\sim$80 °C. A sensible solid cooling time interval follows. As a consequence of the TES discharge, the outlet temperature T_6 has a slower drop with respect to T_5.

Fig. 8(b) shows the air mass flow rate through the TES $\dot{m}_{TES}$, together with the thermal powers $\dot{Q}_{a5}$, $\dot{Q}_{a6}$, $\dot{Q}_{TES}$, Eqs. (1) to (3).

$$\dot{Q}_{a5} = \left(T_5 c_{p5} - T_{amb} c_{p,amb}\right)\dot{m}_{TES} \qquad \text{(eq. 1)}$$

$$\dot{Q}_{a6} = \left(T_6 c_{p6} - T_{amb} c_{p,amb}\right)\dot{m}_{TES} \qquad \text{(eq. 2)}$$

$$\dot{Q}_{TES} = \dot{Q}_{a6} - \dot{Q}_{a5} \qquad \text{(eq. 3)}$$

The power exchanged between the airflow and the TES shows a peak of 6 kW and ranges between 2 kW and 4 kW during latent heating and cooling, depending on the operating conditions.
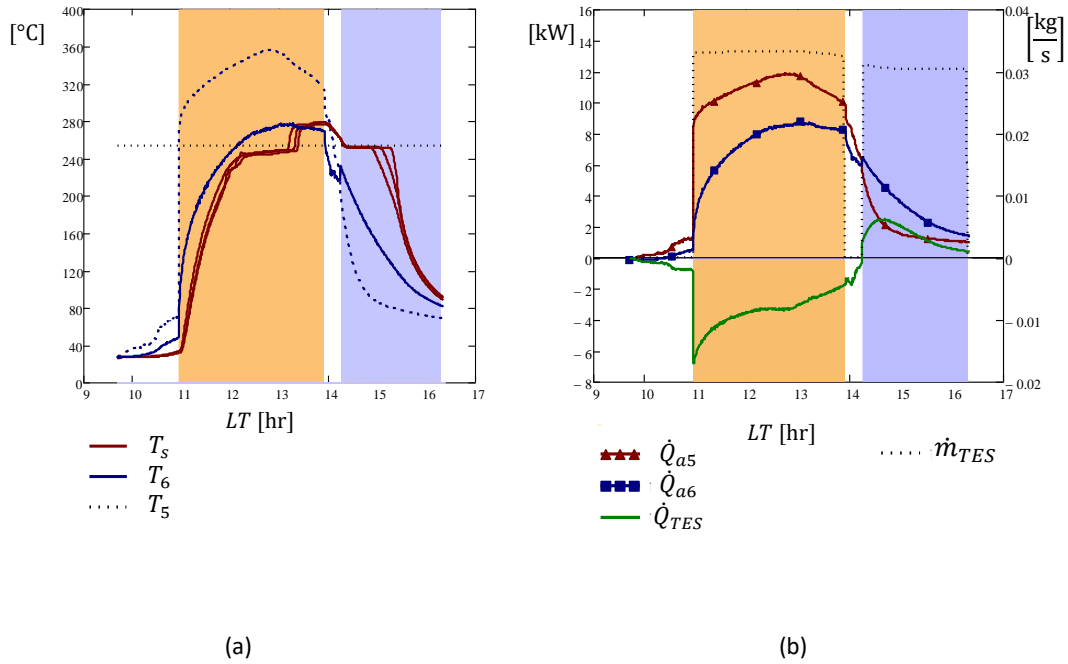
(a)

(b)

Fig. 8. Charging and discharging test. (a) Main temperatures and melting temperature, (b) Thermal power and mass flow rate vs. Local Time LT.

Sensible and latent heat stored during the charging process can be estimated from thermophysical properties of the salt and its container. During sensible heating when at solid-state from ambient temperature (30 °C) to salt melting temperature (254 °C), the overall amount of salt can store $Q_{salt}^{sol} = 1.25$ kWh of heat, considering an average specific heat capacity of 0.414 Wh/kg K, (1.49 kJ/kg K). Considering the specific latent heat of 0.1 kWh/kg (360 kJ/kg), the latent heat stored during complete melting results $Q_{salt}^{mel} = 1.348$ kWh.

The amount of heat stored in the salt during charging, up to complete melting is $Q_{salt} = Q_{salt}^{sol} + Q_{salt}^{melt} = 2.6$ kWh.

The sensible heating of the finned tubes containing the salts is not negligible. The mass of the stainless-steel tube is 3.37 kg, in addition to the 5.7 kg of carbon steel fins. Considering an average specific heat of 0.5 kJ/kg K, the four finned tubes stores $Q_{cyl} = 1.108$ kWh of heat when heated from ambient to salt melting temperature, corresponding to 30% of the amount of heat stored in the salt and finned tube container $Q_{TES,ch}^{cal} = Q_{salt} + Q_{cyl} = 3.7$ kWh.

An experimental estimation of $Q_{TES,ch}^{exp}$ can be obtained by integrating over the charging time τ (excluding liquid heating) the $\dot{Q}_{TES}$ of Eq.3, reported in Fig.8(b).

$$Q_{TES,ch}^{exp} = \int_{\tau_0}^{\tau_m} \dot{Q}_{TES}\langle\tau\rangle\, d\tau \qquad\qquad \text{(eq. 4)}$$

A value of $Q_{TES,ch}^{exp} = 9.14$ kWh is found between the time of charging start τ_0 and the time of complete salt melting τ_m. The much higher value of $Q_{TES,ch}^{exp}$ than $Q_{TES,ch}^{cal}$ is due to heat exchange between airflow and the TES external case. Although the losses to ambient are minimized by the mineral wool thermal insulation, both the square air channel walls and the insulation itself increase their temperature during the charging period, storing a non-negligible amount of heat.

Additional features of melting and solidifying processes can be observed in Fig. 9 (a). It reports, besides three internal salt temperatures $T_{s,up}, T_{s,c}, T_{s,do}$, the temperature of the salt layer adjacent to the wall $T_{w,up}, T_{w,do}$ as in Fig. 9(b).
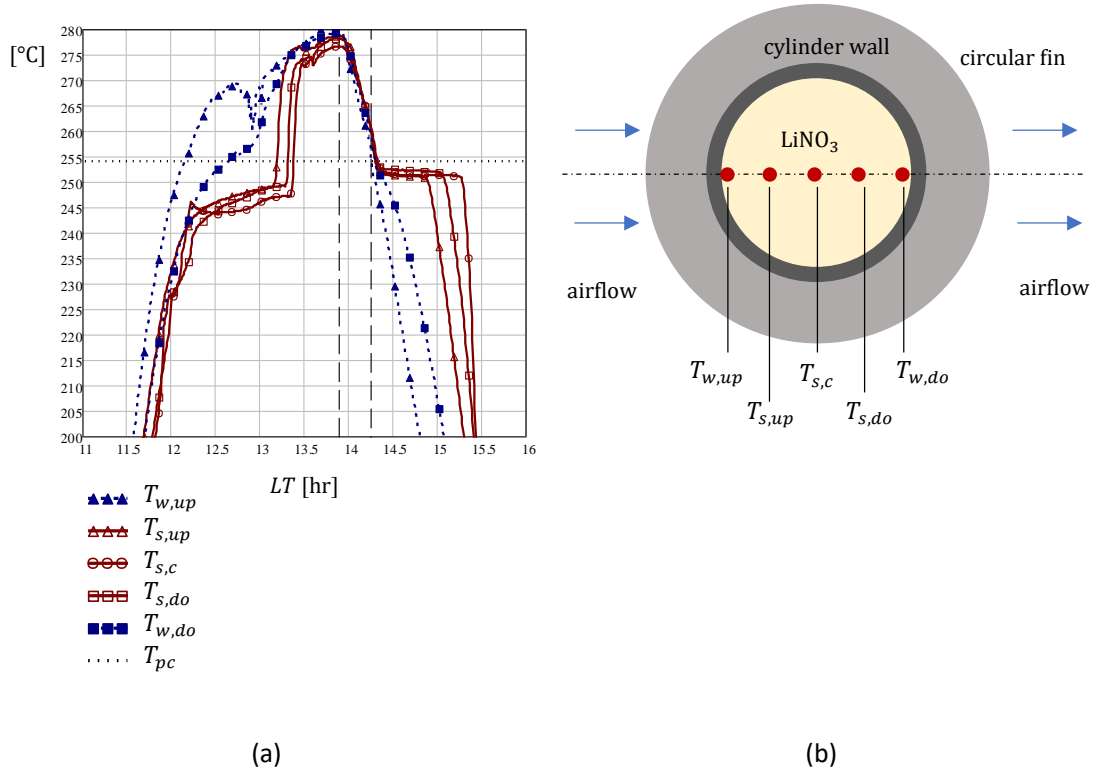
(a) (b)

Fig. 9. The salt temperature during melting and solidification. (a) Temperatures vs Local Time LT, (b) sensors position.

As expected, the salt temperature adjacent to the upstream wall $T_{w,up}$ reaches the melting point at first, followed by the salt temperature at the opposite site $T_{w,do}$. The salt starts to melt from the external layer adjacent to the hot wall of the cylinder, while the core of the salt block is still a few degrees below the melting point. The limited thermal conductivity of the solid salt $k_{salt}^{sol} = 1.348$ W/K m controls the heat transfer to the salt core and the melting front speed from the outer surface to the inner core.

The core temperatures $T_{s,up}, T_{s,c}, T_{s,do}$ grow smoothly during the melting process, below the theoretical melting temperature $T_{pc} = 254$ °C. The center temperature $T_{s,c}$ is the lowest and the last, which start to raise again for liquid sensible heating. A similar trend is observed during the solidifying process. The wall temperatures $T_{w,up}$ and $T_{w,do}$ drops as first. Then, internal temperatures keep steady around 252 - 253 °C. They are much closer between them than in the melting case, depicting a more homogeneous process. This can be an effect of the higher liquid salt thermal conductivity with respect to solid, $k_{salt}^{liq} = 2.96$ W/K m. Moreover, solidification progresses from the outer surface to the inner core.

The subcooling phenomenon, a typical effect that delays the solidification of some phase change materials, is not observed in our case.

The second test performed considers the joint behavior of T-SAH and the TES. The TES is connected permanently in series with the T-SAH as in Fig.1. From the time when the solar field begins to track the sun, either the T-SAH and the TES undergo a heating transient, which brings up the air temperature at the TES inlet (turbine outlet) T_5 as in Fig. 10(a). The outlet TES temperature T_6 grows slower and below T_5. After sensible heating of about 2 h, the salt starts melting. Liquid sensible heating takes place as the final step of the charging process, up to 290 °C of salt temperature. Then, the solar field is defocused to simulate a short sun power interruption, as during the appearance of clouds.

Due to the thermal inertia of T-SAH components (pipes, receiver tubes, turbocharger) the temperature drops at the TES inlet T_5 is not instantaneous and the airflow keeps heating the TES for a few minutes. Then it starts to discharge the TES, which begins to solidify. Its effect on the outlet temperature T_6 can be noticed, which remain above 180 °C during a sun power shortage of 45 min, while T_5 drops down to 120 °C.

Subsequently, the sun tracking is restored. The salt keeps solidifying for a few minutes before it starts to melt again, afterwards heated as a liquid. The last part of the experiment is again a full TES discharge. Globally,

the effect of the TES charging and discharging thermal capacity is smoothing the variation of outlet air temperature T_6 with respect to T_5, which would be the delivery in the absence of TES. Fig.10 (b) reports the exchanged power $\dot{Q}_{TES}$ as well as the solar power gain across the solar field $\dot{Q}_u$ and the power $\dot{Q}_{a5}$ and $\dot{Q}_{a6}$.

(a)   (b)
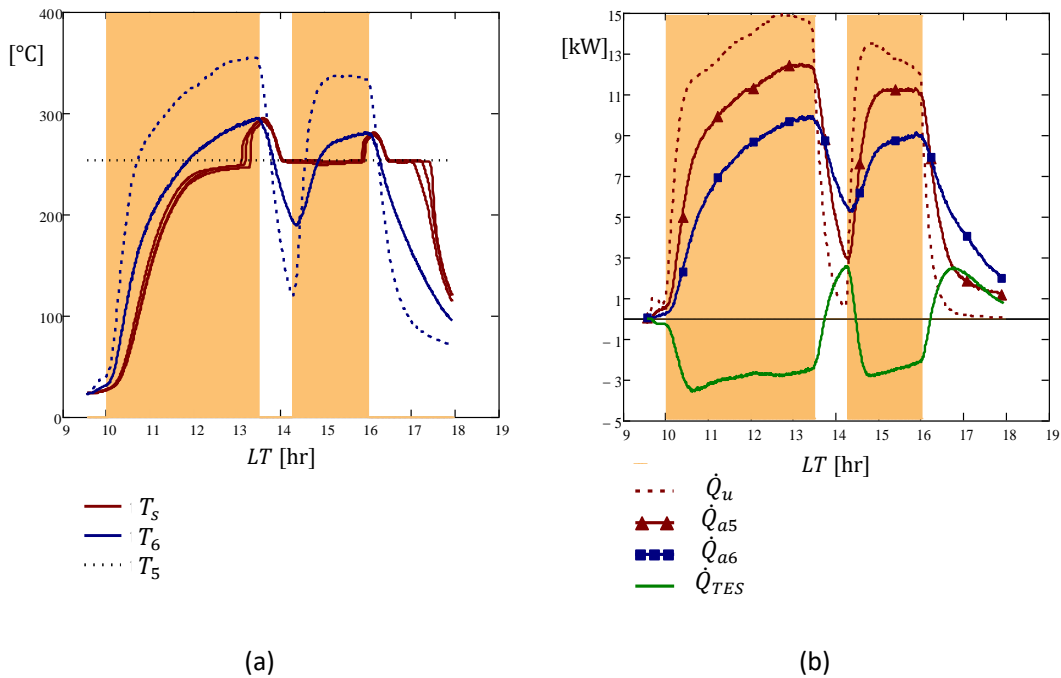
Fig. 10. Effect of TES on delivery hot airflow. (a) Temperature. (b) Thermal power vs Local Time LT.

4. Conclusions

The results obtained during the first experimental tests carried out on the TES unit indicate the viability Lithium Nitrate as phase change material for the range of temperatures typical of the new turbo-assisted solar air heater T-SAH experimented. The shell-and-tube configuration selected for the heat exchanger design, seems a suitable solution, aiming at compactness, simplicity and low-cost, by using commercial finned tubes and air conduits.

The experiments indicate that more than one row of vertical tubes would be needed for increasing the storage capacity and the beneficial effect of TES on T-SAH outputs.

An extensive thermal analysis would be convenient for characterizing the heat transfer phenomena taking place, through the development of a comprehensive numerical model. The experimental data provided would represent a useful information for the numerical model tuning and validation.

5. References

Crespo, A. et al. (2018) 'Latent thermal energy storage for solar process heat applications at medium-high temperatures – A review', Solar Energy, (June), pp. 1–32. doi: 10.1016/j.solener.2018.06.101.

Famiglietti, A. et al. (2020) 'Direct solar production of medium temperature hot air for industrial applications in linear concentrating solar collectors using an open Brayton cycle . Viability analysis', 169(September 2019). Available at: https://doi.org/10.1016/j.applthermaleng.2020.114914.

Famiglietti, A. et al. (2021) 'Turbo-assisted direct solar air heater for medium temperature industrial processes using Linear Fresnel Collectors . Assessment on daily and yearly basis', 223. Available at: https://doi.org/10.1016/j.energy.2021.120011.

Famiglietti, A. and Lecuona, A. (2021a) 'Direct solar air heating inside small-scale linear Fresnel collector assisted by a turbocharger : Experimental characterization', Applied Thermal Engineering, 196(September).

doi: 10.1016/j.applthermaleng.2021.117323.

Famiglietti, A. and Lecuona, A. (2021b) 'Small-scale linear Fresnel collector using air as heat transfer fluid: Experimental characterization', Renewable Energy, 176, pp. 459–474. doi: 10.1016/j.renene.2021.05.048.

Sharma, A. K. et al. (2017) 'Solar industrial process heating: A review', Renewable and Sustainable Energy Reviews, 78(December 2016), pp. 124–137. doi: 10.1016/j.rser.2017.04.079.

Solatom (accessed 01/09/2021) SOLAR STEAM FOR INDUSTRIAL PROCESSES. Available at: http://www.solatom.com/.

Tamme, R.; Bauer, T.; Buschle, J.; Laing, D.; Müller-Steinhagen, H.; Steinmann, W. D. (2008) 'Latent heat storage above 120 C for applications in the industrial process heat sector and solar power generation.', International Journal of energy research, 32(3), pp. 264–271. doi: 10.1002/er.

www.chemicalbook.com (accessed 01/09/2021). Available at: https://www.chemicalbook.com/ChemicalProductProperty_EN_CB7400757.htm.